UC Davis
UC Davis Previously Published Works

Title

Prototype Small-Animal PET-CT Imaging System for Image-Guided Radiation Therapy

Permalink

https://escholarship.org/uc/item/51b0b82t

Authors

Mikhaylova, Ekaterina
Brooks, Jamison
Zuro, Darren M
et al.

Publication Date

2019

DOI

10.1109/access.2019.2944683

Peer reviewed

Prototype Small-Animal PET-CT Imaging System for Image-guided Radiation Therapy

Ekaterina Mikhaylova[1], **Jamison Brooks**[2,3,#], **Darren Zuro**[2,3,#], **Farouk Nouizi**[4,#], **Maciej Kujawski**[5], **Srideshikan Sargur Madabushi**[2], **Jinyi Qi**[1], **Mengxi Zhang**[1], **Junie Chea**[6], **Erasmus K. Poku**[6], **Nicole Bowles**[6], **Jeffrey Y. C. Wong**[2], **John E. Shively**[5], **Paul J Yazaki**[5], **Gultekin Gulsen**[4], **Simon R. Cherry**[1], **Susanta Hui**[2]

[1]Department of Biomedical Engineering, University of California Davis, Davis, CA 95616 USA

[2]Department of Radiation Oncology, City of Hope, Duarte, CA 91010, USA

[3]Department of Radiation Oncology, University of Minnesota, Minneapolis 55455, MN

[4]Department of Radiological Sciences, University of California Irvine, Irvine, CA 92697, USA.

[5]Molecular Imaging and Therapy, City of Hope, Duarte, CA 91010, USA.

[6]Radiopharmacy, City of Hope, Duarte, CA 91010, USA

Abstract

Molecular imaging is becoming essential for precision targeted radiation therapy, yet progress is hindered from a lack of integrated imaging and treatment systems. We report the development of a prototype positron emission tomography (PET) scanner integrated into a commercial cone beam computed tomography (CBCT) based small animal irradiation system for molecular-image-guided, targeted external beam radiation therapy. The PET component consists of two rotating Hamamatsu time-of-flight PET modules positioned with a bore diameter of 101.6 mm and a radial field-of-view of 53.1 mm. The measured energy resolution after linearity correction at 511 KeV was 12.9% and the timing resolution was 283.6 ps. The measured spatial resolutions at the field-of-view center and 5 mm off the radial center were 2.6 mm × 2.6 mm × 1.6 mm and 2.6 mm × 2.6 mm × 2.7 mm respectively. ^{18}F-Fluorodeoxyglucose-based PET imaging of a NEMA NU 4–2008 phantom resolved cylindrical volumes with diameters as small as 3 mm. To validate the system in-vivo, we performed ^{64}Cu-DOTA-M5A PET and computed tomography (CT) imaging of carcinoembryonic antigen (CEA)-positive colorectal cancer in athymic nude mice and compared the results with a commercially available Siemens Inveon PET/CT system. The prototype PET system performed comparably to the Siemens system for identifying the location, size, and shape of tumors. Regions of heterogeneous ^{64}Cu-DOTA-M5A uptake were observed. Using ^{64}Cu-DOTA-M5A PET and CT images, a Monte Carlo-based radiation treatment plan was created to escalate the dose to the ^{64}Cu-DOTA-M5A-based, highly active, biological target volume while

Corresponding Author: Susanta Hui (shui@coh.org).

#indicates equal work was performed

largely sparing the normal tissue. Results demonstrate the feasibility of molecular-image-guided treatment plans using the prototype theranostic system.

Index Terms—

molecular imaging; multimodal imaging; targeted radiation; theranostic

I. Introduction

Molecular imaging has great potential to improve the use of external beam radiation therapy for the treatment of cancer by better identifying cancer-specific targets, enhancing the design of targeted radiation delivery to the target, monitoring response to treatment, and minimizing collateral damage to normal tissue [1, 2]. The use of such imaging to support more precise radiation targeting to the biological target volume (BTV) is increasingly becoming a focus of radiation research as it allows for further dose escalation to BTV based tumor subregions [3–5]. However, single platform systems capable of both molecular diagnostic and targeted external beam radiation therapy treatment techniques (i.e. theranostics) are not widely, or commercially available for preclinical animal research.

The lack of preclinical integrated technology that easily provides molecular imaging, anatomic information, and targeted treatment makes it difficult to accurately administer precise targeted radiation treatments for plans that are based off of both molecular and anatomical images. Co-registration errors among standalone imaging modalities limit knowledge of the exact size and shape of tumors. A lack of equipment with integrated molecular imaging modalities (positron emission tomography [PET] and optical imaging) limits head-to-head comparison of the anatomical target volume (ATV) obtained by computed tomography (CT) imaging and biological target volume (BTV) obtained by molecular imaging. Being able to define both the ATV and BTV in a preclinical targeted radiation therapy system would enable targeted radiation therapy based off of both of these regions, where a boost to regions of the tumor with high biological activity could be performed. This will allow for investigation into the use of functional-based molecular imaging to determine radiation dose.

To address this need, we sought to develop a multi-modal theranostic imaging instrument, which we called multimodal-imaging, radiation response, and operation research system (MIRRORS). Here we report a prototype instrument that includes a PET imaging system integrated with a commercial cone beam computed tomography (CBCT) and dose calculated targeted radiation treatment system. To validate biological tumor imaging using PET in this feasibility study, we used our previously developed anti-carcinoembryonic antigen (CEA) monoclonal antibody M5A lined with the radioisotope Cu-64 via the chelator tetra-azacyclododecanetetra-acetic acid (DOTA) [6]. The CEA antigen is highly expressed (>90%) in many solid tumor malignancies (colon, pancreas, lung, and breast) [7–9], making it ideal for these studies. We then compared data acquisition and image quality using the prototype with those features of a commercially available Siemens Inveon PET/CT. Reconstructed images using MIRRORS were comparable to images obtained from the

Siemens system for tumor visualization. Simulations of radiation treatment plans were performed based on MIRRORS obtained images of high CEA tumor expression. The simulations demonstrate the feasibility of using molecular information for differential dose painting, which involves dose escalation to the high-CEA region without increasing the dose to normal tissues.

II.   Materials and Methods

A.   Evaluation of Performance of Pet Modules in Mirrors

The PET insert was composed of two rotating Hamamatsu TOF-PET modules (EVA.KIT1-DEMO C13500–4075LC-12 type) (Fig. 1A) [10], each of which comprised a 12×12 array of lutetium fine silicate (LFS) scintillating crystals. Each crystal was 4 mm $\times$ 4 mm $\times$ 20 mm with a pixel pitch of 4.205 mm. The scintillator signal was read by a 12×12 array of 4 mm $\times$ 4 mm multi-pixel photon counter photodetectors using 1–to–1 coupling. The two PET modules were placed on a rail holder, which allowed for adjustable distance between the modules (Fig. 1B–C). The rail holder was installed on the gantry of an X-RAD SmART system (Precision X-ray Inc., CT) (Fig. 1B–C). The radial field of view (FOV) was equal to the length of the modules (53.1 mm). The axial FOV (the distance between the PET modules) was set to 101.6 mm (4 inches). The CBCT FOV is at a different bed position in the radial direction (z) than the PET FOV, allowing for independent data collection to occur by moving the motorized bed without repositioning the animal. The small animal bed with 3-dimensional (3D) mechanical positioning was used to position the animal at the isocenter of the PET modules. The distance between detectors and the bed was kept as small as possible to maximize solid angle coverage, which improved PET sensitivity.

The Hamamatsu acquisition software records events as singles. The recorded data includes energy of a detected gamma ray, its time stamp, and the crystal ID. The single events were then post-processed using our locally developed coincidence-sorting software to form a list of coincidences for subsequent image reconstruction. The coincidence window was set to 3 ns.

All point source performance evaluation measurements were taken using low-activity (<10 μCi) approximately 0.3-mm-diameter point-sources. Calibration, energy resolution, and timing resolution data acquisitions were performed at room temperature. without rotating the PET modules. A total of 10 million single events were acquired and post-processed for each test.

B.   Phantom Imaging

We used a standard NEMA small animal phantom for this study as described in the NEMA NU 4–2008 protocol (Fig. 2) [11, 12]. The phantom consisted of three parts: two lids, the main body chamber, and five 20-mm-long cylindrical rods of 1, 2, 3, 4, and 5 mm in diameter. The top lid contained two 14-mm-long cylindrical chambers of 8 mm diameter. The main body chamber of the phantom, as well as the cylindrical rods, were filled with ^{18}F-fluorodeoxyglucose solution (100 $\pm$ 5 μCi) initial total activity, while the two chambers in the top lid contained air and non-radioactive water.

The phantom was then placed on the animal bed, which was located in the center of the rotating PET system such that the axis of its main body was aligned with the radial FOV of the scanner. Data was acquired for 5 min at each module angular position, collecting approximately 10 million single events per angle with a total scan time of approximately 20 min. Data, acquisition was done using a total of four discrete positions of the PET modules (0°, 45°, 90°, and 135° angles) around the phantom. The four module positions covered the full 2π of the radial FOV. Data acquisition was performed at room temperature; no cooling systems were needed. To facilitate image reconstruction, we collected data only at the stationary module angles, but not during module rotation. Imaging performance of the PET system was tested using the NEMA NU 4–2008 standard guidelines for image quality measurements [11].

The image was reconstructed using a sinogram-based 3D maximum-likelihood expectation maximization (ML-EM) algorithm over 30 iterations [13]. The system matrix was precomputed by dividing each crystal into $10 \times 10 \times 5$ sub-elements to perform the numerical volume integration using Siddon's method [14]. The sensitivity image was computed by back projection of the sinograms [15, 16]. The image voxel size was set to 1.05 mm $\times$ 1.05 mm $\times$ 1.05 mm and the image matrix size to 41 voxels $\times$ 41 voxels $\times$ 49 voxels. No data corrections, for random, scattered, attenuation, data normalization, or point-spread-function modeling, were applied. Due to limited solid angle coverage of the detector system, all events above the lower energy threshold (100 keV) and within a 3 ns timing window were accepted. This ensured as many coincidences were captured as possible for image reconstruction. To evaluate image quality, we computed the recovery coefficients (RCs) for the five cylindrical volumes, calculated by dividing the reconstructed count density by the true count density. Additionally, we evaluated the uniformity of the phantom's main body, and the spillover ratio (SOR) using NEMA NU 4–2008 standard procedures [11].

C. In-Vivo Imaging

To evaluate the in-vivo imaging capability of the MIRRORS system, we imaged CEA-positive colorectal cancer in mice. All mouse studies were conducted under a City of Hope Institutional Animal Care and Use Committee approved protocol. Two athymic nude mice were injected subcutaneously with MC38-CEA cells (10^6 cells in a total volume of 50 μl). Once tumors reached a size of approximately 150 mm^3, mice were injected with 93.5 $\pm$ 4.5 μCi of ^{64}Cu-DOTA-M5A radiolabeled antibody that binds to CEA-expressing cells. The anti-CEA antibody M5A was conjugated with NHS-DOTA as previously described [17]. Preliminary PET scans of ^{64}Cu-DOTA-M5A tumor uptake were performed 43–44 h post-injection using a Siemens Inveon PET/CT system. Approximately 10 h after being imaged using the Siemens Inveon system, the same two mice were imaged using MIRRORS for comparison.

For imaging using MIRRORS, the mouse was placed at the isocenter of the integrated system. The radial axis (z) of the mouse body was aligned with the radial FOV (z) of the MIRRORS. The tumor position was chosen as close as possible to the center of the radial FOV, such that the system could completely capture the tumor. The total scan time was 54

min. The same data acquisition positions were used as with the NEMA NU4–2008 small animal phantom.

MIRRORS based PET acquisition collected approximately 10 million single events at each angle, thus acquiring a total of 40 million single events per tumor. This resulted in ~600,000 coincidence events, which is substantially fewer events than are normally desired for mouse imaging (typically ~10 million or more). In order to maximize coincidence events, no energy window was applied to the data. However, this led to noise events, which deteriorated overall image quality. Image reconstruction was done using the same method as above for the NEMA NU4–2008 small animal phantom.

The Siemens Inveon PET/CT images were reconstructed using a two-dimensional OSEM algorithm (Siemens Inveon™, Munich, Germany) [13, 18] after acquiring a total of approximately 9 million coincidences over a scan duration of 60 min. The increased coincidences of the Siemens Inveon compared to the MIRRORS system is due to the increased solid angle coverage of the ring-shaped detector setup compared to the rotating modules. The energy window of the Siemens system was set to 350–650 keV and the data was corrected for isotope decay and dead time. Fusion, registration, and analysis of PET/CT image sets obtained from MIRRORS and analysis of the Siemens Inveon system were performed using VivoQuant®(In-Vicro, Boston, MA) software.

D. Molecular Image Guided Radiation Treatment (MIGRT) Simulation

Registered PET/CT images of mice were imported into Velocity™(Varian Palo alto, CA) and the anatomical target volume with a 2 mm margin (ATV) was contoured based on CBCT images. A subregion of the ATV was contoured based off ^{64}Cu-DOTA-M5A images of high tumor uptake, defined as highly active biological volume (hBTV). Contoured volumes were used to simulate a radiation treatment plan using a Monte Carlo dose calculation software based on the EGSnrc/DOSXYZnrc [19]. This plan could be applied directly to the X-RAD SmART system for tumor treatment. ATV based treatment simulations were performed using opposing lateral 10 mm × 10 mm square beam x-ray fields at 225 kVp and 13 mA. The central axis dose of a 10 mm × 10 mm square beam X-ray field at 21.4 mm depth in solid water is approximately 63% of the maximum depth dose. Since tumors are superficial, this allowed for a fairly homogeneous dose distribution using opposing lateral beams. A boost to the hBTV was simulated using a second set of opposing lateral 5 mm × 5 mm circular beams. Dose calculations were performed at the center of the respective target volumes. For dose calculation purposes, normal tissue was defined as non-tumor tissue located at least 5 mm away from the tumor center, outside of the ATV.

III. Results

A. Evaluation of Performance of Pet Modules in Mirrors

Before assessing the 3D based imaging capabilities of the system, we performed energy spectrum linearity calibrations, measured the systems energy resolution, evaluated the timing resolution, and measured the spatial resolution of the PET modules.

1) Energy Spectrum Linearity Calibration: We used a linearity calibration to correct the energy spectrum of each crystal. The linearity test was performed by placing several low-activity (<10 μCi) point sources at the center of module's FOV. The point sources used and their corresponding peaks were: [57]Co, peak at 122 keV; [22]Na, two peaks at 511 keV and 1274 keV; and 137Cs, peak at 662 keV. The energy spectrum histogram of a single crystal of PET module "A" and the crystal's corresponding linearity plot are shown in Fig. 3. Coincidence energy histograms were acquired for each PET crystal and corrected for non-linear detector response. To perform the correction, a cubic spline interpolation of the measured and expected energy peaks is applied to correct each pixel value [20]. The observed characteristics were consistent with expected results and were used for energy spectrum correction.

2) Energy Resolution: After the linearity calibration for each crystal, the individual crystal energy spectra could be summed into a single energy spectrum to calculate the overall energy resolution of the PET detection system. To assess energy resolution, we used a 10 μCi [22]Na point-source placed at the FOV center. The energy histograms of all the calibrated crystals were summed to obtain the overall PET system coincidence energy spectrum (Fig. 4). A Gaussian function was fit to the 511 keV peak of the energy spectrum histogram. The percentage ratio of the full width at half maximum (FWHM) to the Gaussian peak value was calculated as a measurement of the energy resolution and was found to be 12.9%. This value is typical for LFS and lutetium oxyorthosilicate (LSO) based detector systems [21].

3) Timing Resolution: The timing resolution between the two PET modules was obtained using the "PET Module analysis application "Var 1.0.0.3" software provided by Hamamatsu. The resulting two-module-system timing resolution was 283.6 ps. This timing resolution corresponded to a photon travel distance of ~85 mm, which is larger than a mouse body. Since the time of flight feature of the Hamamatsu EVA-KIT1 DEMO PET modules only enhances the spatial resolution for distances larger than the timing resolution distance of the two PET modules (85 mm), it was not advantageous for mouse imaging, and was not used for image reconstruction.

4) Spatial Resolution: To evaluate spatial resolution, we placed a 10 μCi ~0.3-mm-diameter [22]Na point-source at different positions: at the center of the FOVs (Fig. 5), at the center of the axial FOV but 5 mm off-center radially (Fig. 6), and at several positions along the radial direction with a step of 5 mm (Fig. 7). The image of the point source was reconstructed using a simple back projection method [15, 16] without applying any filter or smoothing. We obtained 163,000 coincidences at the FOV center and 116,700 coincidences at the second position 5 mm off the FOV center radially. The spatial resolution was calculated as the FWHM of a fitted Gaussian function to corresponding line profiles. The resulting radial spatial resolution was ~2.6 mm both at the FOV center and at 5 mm off the radial center. The axial spatial resolution was ~1.6 mm at the radial center and ~2.7 mm 5 mm off the radial center. The reconstructed point spread function at different source positions and their line profiles are shown in Figures. 5–7. The results demonstrate that the

PET modules can produce quality data for localizing and reconstructing an object with a dimension 2.6 mm including the objects placed at the edge of the radial FOV.

B. Phantom Imaging

We used a NEMA NU4–2008 phantom to assess image quality and evaluate the imaging performance of the PET modules. Images of the phantom were reconstructed after acquiring a total of ~12.5 million coincidences using a sinogram-based 3D maximum-likelihood expectation maximization MLEM algorithm. Reconstructed slices of the NEMA NU4–2008 phantom are shown in Fig. 8A–C. Fig. 8D shows the recovery coefficients for a range of line source diameters. Table 1 summarizes and compares the calculated RC, SOR and uniformity region minimum, maximum and mean values. Overall, radioactive cylindrical volumes with diameters as small as 3 mm could be resolved, which agreed with spatial resolution measurements.

C. In-Vivo Imaging

To evaluate MIRRORS for in-vivo small animal imaging, we performed imaging of athymic mice bearing CEA-positive colorectal cancer. Two CEA-positive tumor-bearing mice were injected with the antibody-based anti-CEA imaging agent ^{64}Cu-DOTA-M5A and imaged using both the Siemens Inveon PET/CT and the prototype MIRRORS systems (Fig. 9 A–B). The activity of ^{64}Cu-DOTA-M5A for mice at the start of the MIRRORS PET image acquisition was lower than activity at the start of the Siemens Inveon PET image acquisition because the images were taken approximately 10 h apart (Mouse 1 had an initial calculated activity of 8.12 μCi and 4.59 μCi for the Siemens Inveon PET/CT and MIRRORS system respectively). Table 2 summarizes and compares the data acquisition conditions for Siemens Inveon PET setup [22] and for the MIRRORS insert, showing several advantages of the Siemens system. However, images obtained using the simple MIRRORS prototype could identify the tumor location, size, and shape despite the reduced solid angle coverage due to the smaller active detector area.

Ratios of the maximum intensities for tumor vs. liver were similar between systems. Mouse one had tumor max to liver max ratios of 1.15 and 1.06 for the MIRRORS and Siemens systems respectively, while mouse two had ratios of 0.71 and 0.91. Similar activity ratios from both systems for the mice suggest reliable image acquisition and reconstruction of the MIRRORS system. Interestingly, one CEA tumor (Fig. 9B, mouse 2) showed heterogeneous uptake of ^{64}Cu-DOTA-M5A suggesting an elevated concentration of CEA positive tumor cells in a subvolume of the tumor. This information led us to develop molecular image guided radiation treatment (MIGRT) with the intent to deliver more conformal increased dose treatments to the highly active biological target volume (hBTV) as described in Results section D.

D. Molecular Image Guided Radiation Treatment (MIGRT) Simulation

Using PET/CT images taken from the MIRRORS system, simulations of two treatments covering the CBCT-based ATV were performed at 10 Gy and 30 Gy doses (Figure 10B). Increases in dose should lead to increased tumor control probability. However, increasing the ATV dose also increases the radiation exposure of surrounding normal tissue by

approximately 3-fold (Fig. 10 A–C). Alternatively, simulations giving 10 Gy to the ATV and an additional 20 Gy to the smaller hBTV in mouse 2, results in a dose to the normal tissue that is almost identical to 10 Gy treatment to the ATV alone. Although such hBTV targeted treatment was feasible for mouse 2, the approach was not feasible in mouse 1, where the hBTV and ATV volume were similar. In this situation, dose escalation may not be feasible without increasing dose to normal tissue.

IV. Discussion

There has long been a need for theranostic imaging in the field of preclinical radiation oncology. To the best of our knowledge we have described the first PET-integrated theranostic system for preclinical use and have demonstrated the feasibility of CEA antigen-specific dose escalation. Further development of MIRRORS is expected to shift the preclinical radiation research paradigm from anatomical, nonspecific, physical tumor and radiation response to treatment response monitoring based on biological molecular imaging agents. The benefits of integrated molecular image-guided radiation therapy (RT) include potential for earlier detection of cancer, functionally guided treatment, and rapid evaluation of biological response to treatment.

This prototype integration of PET modules with an anatomical image-guided precision radiation therapy system offers a cost-effective system design, compared to the cost of separate imaging and treatment platforms. Using off-the-shelf detector modules, we generated preliminary PET images with a spatial resolution of ~2.6 mm. We have also shown MIRRORS has tumor-specific molecular imaging capability, as shown by our ability to reconstruct images of ^{64}Cu-DOTA-M5A to visualize and identify the location, size, and shape of CEA-positive tumors. Both CBCT and PET based images from the MIRRORS system were comparable to those of a Siemens Inveon PET/CT system, establishing the feasibility and utility of the prototype system for the identification of ATV and BTV regions. The primary advantage of this integrated system is the ability to obtain 3D images of molecular agents immediately before treatment, allowing for real-time development of treatment plans based off of a biological target volume. This enables the system to precisely deliver radiation to regions of high biological tumor activity. MIRRORS also provides the ability to measure early (within hours) changes in biological response to radiation, and provides a means to begin to understand physical and biological changes over time for different tumor types and radiation treatment strategies.

Although CT-based anatomical imaging provides precise dose calculation, localization, and delivery guidance to the tumor mass, it does not specifically visualize the biological boundaries of a given tumor or tumor biological heterogeneity. Using MIRRORS, we were able to detect heterogeneity in tumor biology by PET imaging of CEA expression. Additionally, PET imaging was used to simulate dose escalation to a subvolume of the anatomical tumor boundary, a region with high uptake of ^{64}Cu-DOTA-M5A, while minimally increasing dose to the surrounding normal tissue. Results demonstrate the feasibility of MIGRT to spare normal tissues [23–25]. This treatment technique enables PET guided heterogeneous dose increases to at risk tumor subvolumes. MIGRT treatments combined with investigation into the wide variety of molecular agents have the potential to

increase local tumor control and should in turn improve overall survival [3–5]. Molecular imaging will also enable the rapid post assessment of functional tumor changes following radiation therapy.

Although it shows promise, this prototype still has several limitations. 1) the low spatial resolution of the detectors (2.6 mm) limits detection of spatial heterogeneity in tumors smaller than ~ 5 mm in diameter.2) The limited PET solid angle coverage (~0.041 VS. ~0.23 for the Siemens Inveon PET) leads to collection of fewer coincidences than desirable desired for mouse imaging(~0.6 million vs. ~10 million). 3) The low energy threshold and lack of corrections limit quantitative measurements. However, the MIRRORS prototype system provides the proof of concept needed to incorporate a more optimized PET detector geometry within the radiation therapy and CT platform. We are currently developing a next generation system to dramatically improve performance in these areas. Despite limitations, the current MIRRORS prototype demonstrates the feasibility and utility of an integrated molecular imaging and theranostic system.

V. Conclusion and Future Work

The reported results demonstrate a promising prototype molecular image guided theranostic system for radiation therapy. Future development based on this approach will be focused on increasing spatial resolution, increasing sensitivity, and improving solid angle coverage to develop a more robust theranostic system. This can be obtained by using a ring-shaped array of PET detectors. Improving PET imaging resolution and sensitivity will enable better identification of tumor heterogeneity, allowing for more precise dose painting strategies. Future in-vivo studies will be essential to begin to understand the efficacy and optimization of MIGRT treatment strategies in tumor control.

Acknowledgement

References

[1]. Glatstein E, Lichter AS, Fraass BA, Kelly BA, and van de Geijn J, "The imaging revolution and radiation oncology: use of CT, ultrasound, and NMR for localization, treatment planning and treatment delivery," International Journal of Radiation Oncology* Biology* Physics, vol. 11, pp. 299–314, 1985.

[2]. Ling CC, Humm J, Larson S, Amols H, Fuks Z, Leibel S, et al., "Towards multidimensional radiotherapy (MD-CRT): biological imaging and biological conformality," International Journal of Radiation Oncology* Biology* Physics, vol. 47, pp. 551–560, 2000.

[3]. Price PM and Green MM, "Positron emission tomography imaging approaches for external beam radiation therapies: current status and future developments," Br J Radiol, vol. 84 Spec No 1, pp. S19–34, 12 2011. [PubMed: 21427180]

[4]. Lee NY, Mechalakos JG, Nehmeh S, Lin Z, Squire OD, Cai S, et al., "Fluorine-18-labeled fluoromisonidazole positron emission and computed tomography-guided intensity-modulated radiotherapy for head and neck cancer: a feasibility study," Int J Radiat Oncol Biol Phys, vol. 70, pp. 2–13, 1 1 2008. [PubMed: 17869020]

[5]. Zips D, Zophel K, Abolmaali N, Perrin R, Abramyuk A, Haase R, et al., "Exploratory prospective trial of hypoxia-specific PET imaging during radiochemotherapy in patients with locally advanced head-and-neck cancer," Radiother Oncol, vol. 105, pp. 21–8, 10 2012. [PubMed: 23022173]

[6]. Yazaki PJ, Sherman MA, Shively JE, Ikle D, Williams LE, Wong JY, et al., "Humanization of the anti-CEA T84. 66 antibody based on crystal structure data," Protein Engineering, Design and Selection, vol. 17, pp. 481–489, 2004.

[7]. Lwin TM, Murakami T, Miyake K, Yazaki PJ, Shivley JE, Hoffman RM, et al., "Tumor-Specific Labeling of Pancreatic Cancer Using a Humanized Anti-CEA Antibody Conjugated to a Near-Infrared Fluorophore," Annals of surgical oncology, vol. 25, pp. 1079–1085, 2018. [PubMed: 29372363]

[8]. Wong JY, Chu DZ, Yamauchi DM, Williams LE, Liu A, Wilczynski S, et al., "A phase I radioimmunotherapy trial evaluating 90yttrium-labeled anti-carcinoembryonic antigen (CEA) chimeric T84. 66 in patients with metastatic CEA-producing malignancies," Clinical cancer research, vol. 6, pp. 3855–3863, 2000. [PubMed: 11051230]

[9]. Zhu B, Tan IC, Rasmussen JC, and Sevick-Muraca EM, "Validating the sensitivity and performance of near-infrared fluorescence imaging and tomography devices using a novel solid phantom and measurement approach," Technol Cancer Res Treat, vol. 11, pp. 95–104, 2 2012. [PubMed: 22181335]

[10]. Stolin A, Jaliparthi G, Raylman R, Brefczynski-Lewis J, Majewski S, Qi J, et al., "Evaluation of Hamamatsu PET imaging modules for dedicated TOF-capable scanners," IEEE Transactions on Radiation and Plasma Medical Sciences,2019.

[11]. N. E. M. Association, "Performance measurements of small animal positron emission tomographs," NEMA Standards Publication, NU4–2008, pp. 1–23, 2008.

[12]. Mikhaylova E, Kolstein M, De Lorenzo G, and Chmeissani M, "Optimization, evaluation, and comparison of standard algorithms for image reconstruction with the VIP-PET," J Instrum, vol. 9, p. C07004, 7 2014. [PubMed: 25018777]

[13]. Hudson HM and Larkin RS, "Accelerated image reconstruction using ordered subsets of projection data," IEEE transactions on medical imaging, vol. 13, pp. 601–609, 1994. [PubMed: 18218538]

[14]. Siddon RL, "Fast calculation of the exact radiological path for a three-dimensional CT array," Medical physics, vol. 12, pp. 252–255, 1985. [PubMed: 4000088]

[15]. Bruyant PP, "Analytic and iterative reconstruction algorithms in SPECT," Journal of Nuclear Medicine, vol. 43, pp. 1343–1358, 2002. [PubMed: 12368373]

[16]. Kinahan PE, Defrise M, and Clackdoyle R, "Analytic image reconstruction methods," in Emission Tomography, ed: Elsevier, 2004, pp. 421–442.

[17]. Li L, Bading J, Yazaki PJ, Ahuja AH, Crow D, Colcher D, et al., "A versatile bifunctional chelate for radiolabeling humanized anti-CEA antibody with In-111 and Cu-64 at either thiol or amino groups: PET imaging of CEA-positive tumors with whole antibodies," Bioconjug Chem, vol. 19, pp. 89–96, 1 2008. [PubMed: 17988078]

[18]. Shepp LA and Vardi Y, "Maximum likelihood reconstruction for emission tomography," IEEE transactions on medical imaging, vol. 1, pp. 113–122, 1982. [PubMed: 18238264]

[19]. Faddegon BA, Kawrakow I, Kubyshin Y, Perl J, Sempau J, and Urban L, "The accuracy of EGSnrc, Geant4 and PENELOPE Monte Carlo systems for the simulation of electron scatter in

external beam radiotherapy," Phys Med Biol, vol. 54, pp. 6151–63, 10 21 2009. [PubMed: 19779217]

[20]. Knoll GF, Radiation detection and measurement: John Wiley & Sons, 2010.

[21]. Bailey DL, Maisey MN, Townsend DW, and Valk PE, Positron emission tomography: Springer, 2005.

[22]. Visser EP, Disselhorst JA, van Lier MG, Laverman P, de Jong GM, Oyen WJ, et al., "Characterization and optimization of image quality as a function of reconstruction algorithms and parameter settings in a Siemens Inveon small-animal PET scanner using the NEMA NU 4–2008 standards," Nuclear Instruments and Methods in Physics Research Section A: Accelerators, Spectrometers, Detectors and Associated Equipment, vol. 629, pp. 357–367, 2011.

[23]. Bentzen SM and Gregoire V, "Molecular imaging–based dose painting: a novel paradigm for radiation therapy prescription," in Seminars in radiation oncology, 2011, pp. 101–110. [PubMed: 21356478]

[24]. Even AJ, van der Stoep J, Zegers CM, Reymen B, Troost EG, Lambin P, et al., "PET-based dose painting in non-small cell lung cancer: comparing uniform dose escalation with boosting hypoxic and metabolically active sub-volumes," Radiotherapy and Oncology, vol. 116, pp. 281–286, 2015. [PubMed: 26238010]

[25]. Shi X, Meng X, Sun X, Xing L, and Yu J, "PET/CT imaging-guided dose painting in radiation therapy," Cancer Lett, vol. 355, pp. 169–75, 12 28 2014. [PubMed: 25218590]
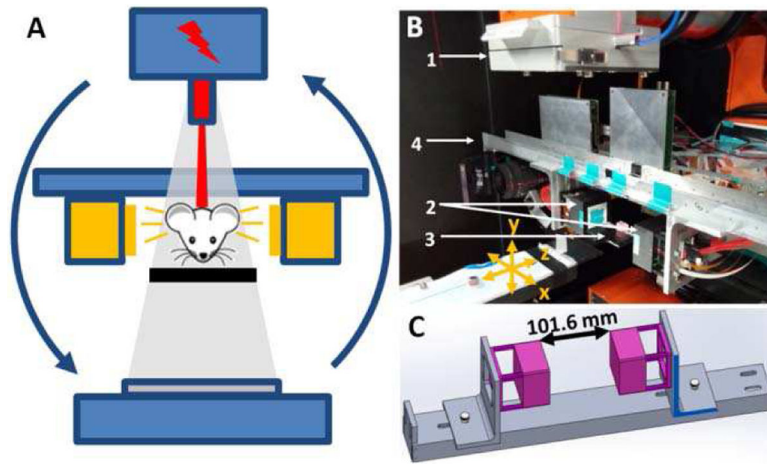
Fig. 1.
Design of MIRRORS prototype. (A) A diagram illustrating the PET detectors setup in the X-RAD SmART system is shown. CBCT detector (Gray), Hamamatsu TOF-PET modules (orange), and X-ray treatment collimator (red), acquire anatomical CT data, acquire molecular PET data, and perform targeted radiation treatments, respectively. The X-RAD SmART gantry and the attached PET modules rotate around the animal allowing for tomographic imaging and treatment. (B) A picture of the PET imaging insert installed in the X-RAD SmART image-guided radiation therapy system depicts (1) the CT X-ray tube, (2) PET modules, (3) Bed for small animals, and (4) rail holder. The axial (x), tangential (y), and radial (z) directions are illustrated in the picture. (C) A Diagram of PET modules placed on a rail holder. The detectors are movable and can slide along the rail holder.
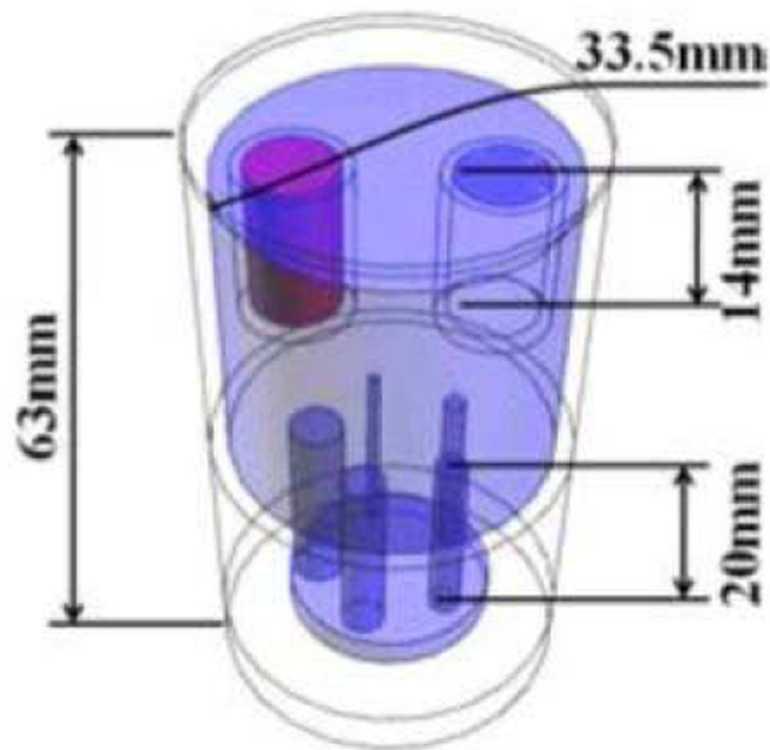
Fig. 2.
Schematic of the NEMA NU4–2008 image quality phantom used for image quality assessment measurements. The five bottom rods and the main body chamber are filled with radioactive water (blue). The two top chambers are filled with air (red) and non-radioactive water (blue). Figure used with permission from another work [12].
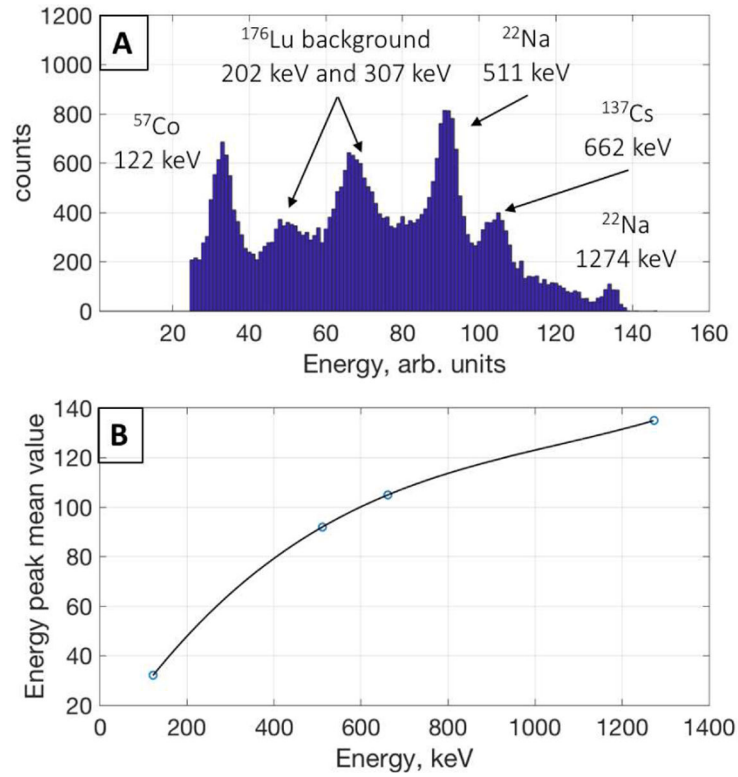
Fig. 3.
Detector energy spectrum and linearity calibration. (A) The energy spectrum for several point sources measured from a single PET crystal (ID 42). The corresponding energy peaks are labeled. The number of counts for each isotope is different due to variation in source activity activity (B) The energy for ^{57}Co, ^{22}Na, ^{137}Cs isotopes are plotted with the detected mean values. The line represents the cubic spline interpolation of the measured and expected energy peaks.
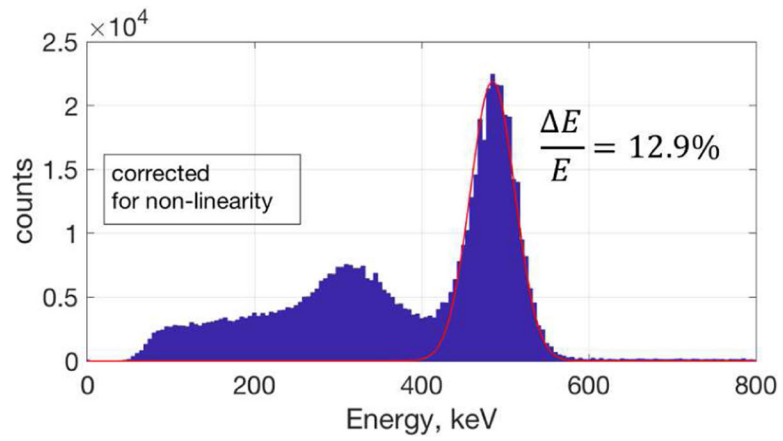
Fig. 4.
Assessment of detector energy resolution. The [22]Na coincidence energy spectrum histogram for the two PET modules after correction for nonlinearity is displayed with its corresponding Gaussian fit.
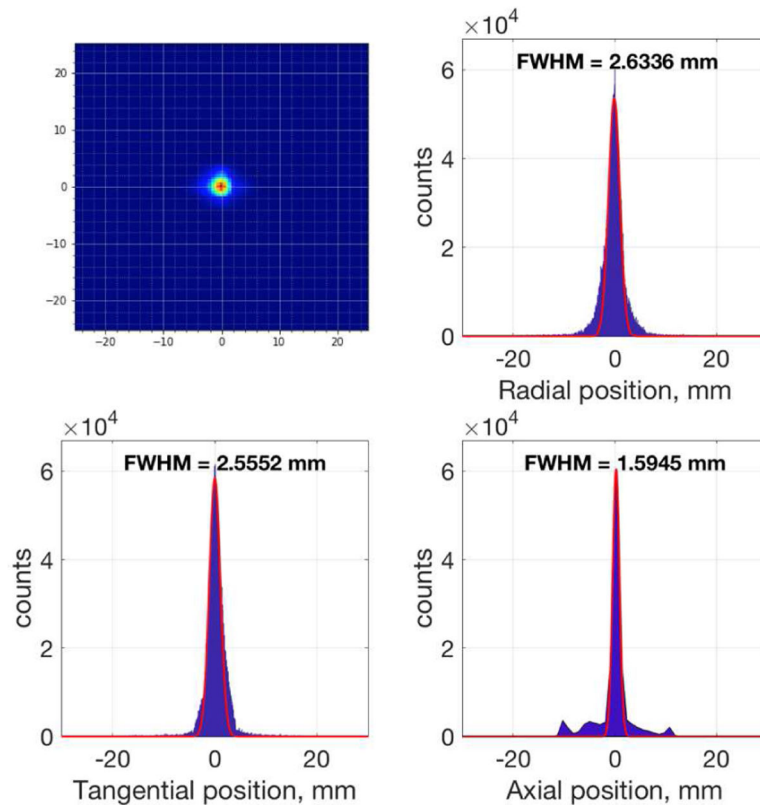
Fig. 5.
Assessment of spatial resolution at the center of the FOV. Three-dimensional reconstructed images of a ^{22}Na point source placed at the center of the axial and radial FOVs and the corresponding line profiles are shown. The FWHM spatial resolutions are equal to 2.6336 mm, 2.5552 mm, and 1.5945 mm in the radial, tangential, and axial directions respectively.
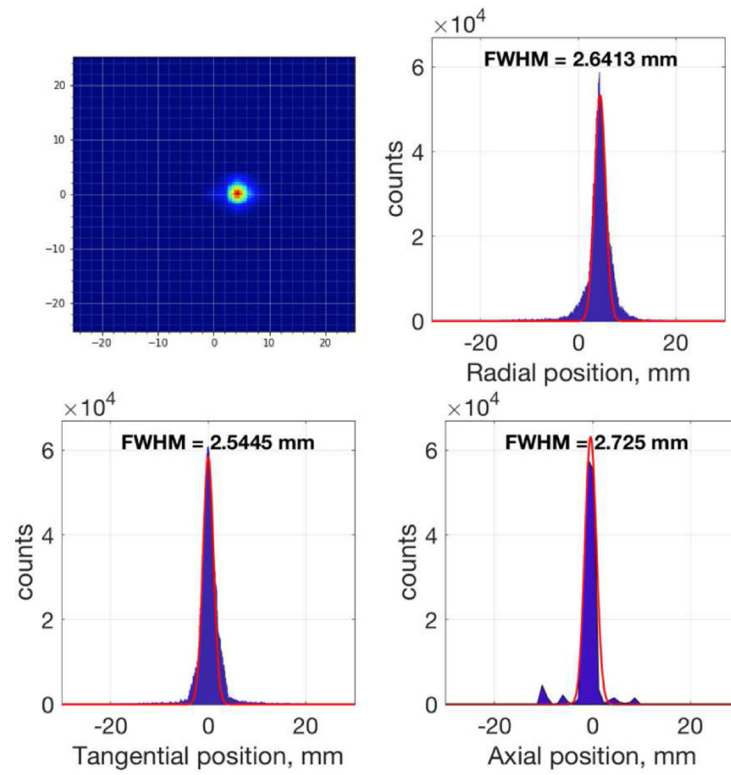
Fig. 6.
Assessment of spatial resolution 5 mm off-center. Three-dimensional reconstructed images of a ^{22}Na point source placed at the axial FOV center and 5 mm off-center radially with the corresponding line profiles are shown. The FWHM spatial resolutions are equal to 2.6413 mm, 2.5445 mm, and 2.725 mm in the radial, tangential, and axial directions respectively.
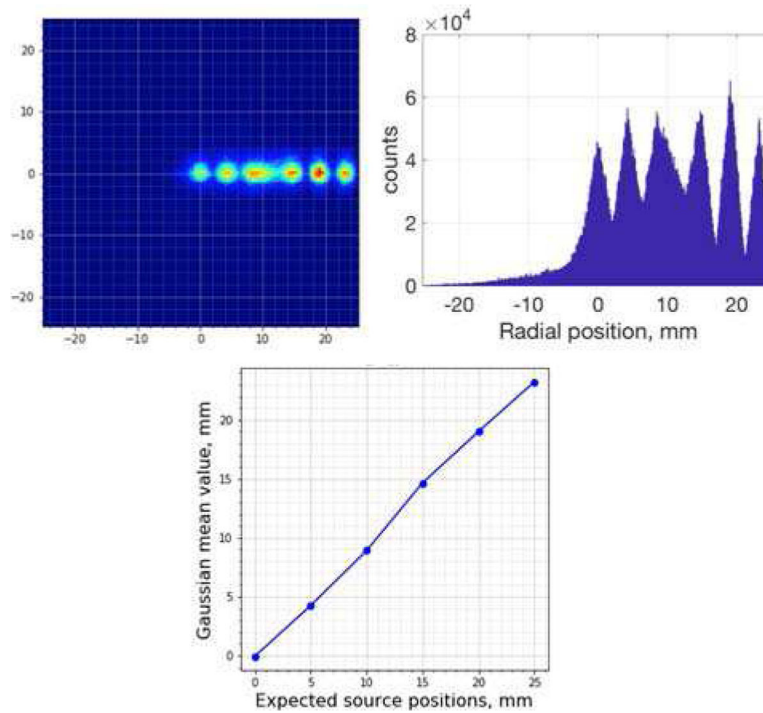
Fig. 7.
Assessment of spatial resolution and position for multiple sources. Three dimensional reconstructed images of several ^{22}Na point sources placed along the radial direction (z) with a 5 mm spacing. (upper left) The corresponding line profile was taken along the radial direction at the axial and tangential center (upper right). The expected source positions are plotted with the position of the Gaussian mean values for each point source comparing the actual spacing and detected spacing of the sources (bottom).
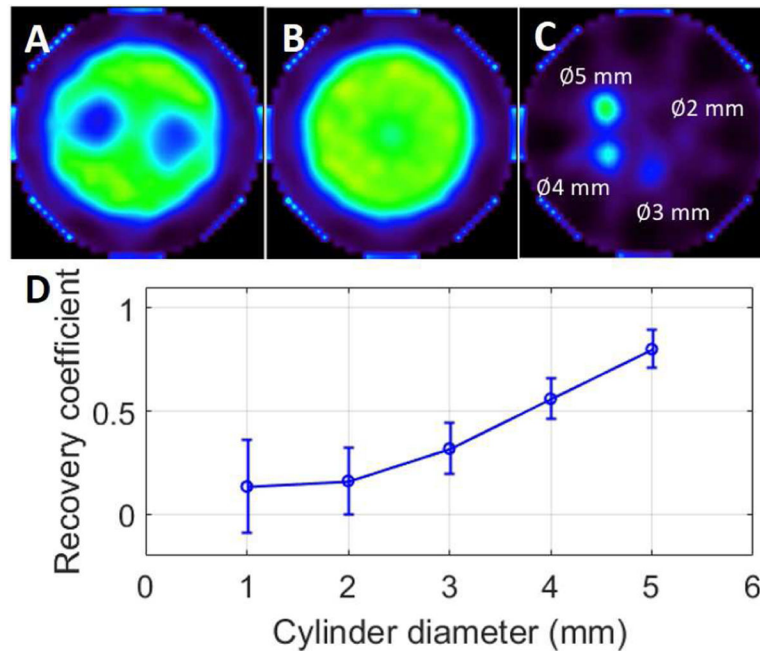
Fig. 8.
Reconstructed NEMA phantom images. Reconstructed images of the NEMA NU4–2008 phantom are shown. (A) The sector of two inserts filled with non-radioactive water and air, (B) the uniform radioactive water sector, and (C) the radioactive water cylindrical volume sector are shown. (D) Recovery coefficients of the radioactive cylindrical volumes are plotted.
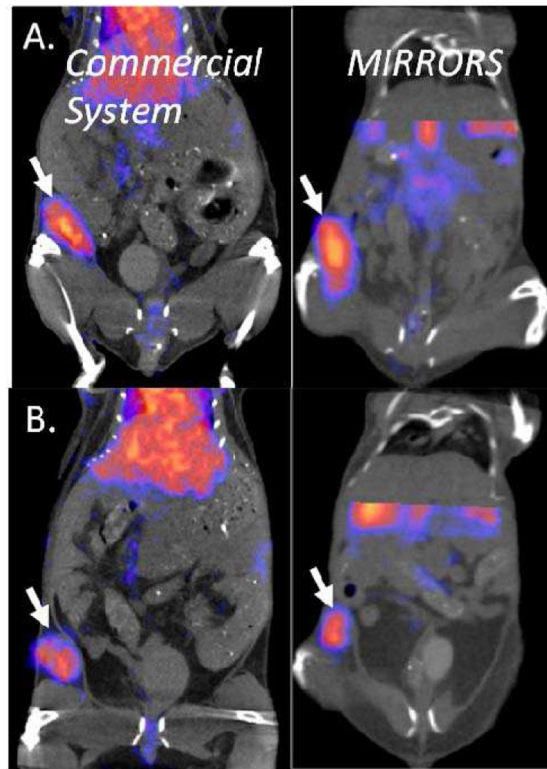
Fig. 9.
64Cu-DOTA-M5A PET/CT image reconstruction in an in-vivo model. Scans of two athymic nude mice performed using a Siemens Inveon PET/CT (Left) and the MIRRORS system (right) for mouse 1 (A) and mouse 2 (B). Images of the same mice on each system were acquired approximately 10 h apart, first using the Siemens system and then on MIRRORS system. White arrows indicate locations of CEA-positive colorectal tumors. Lung activity visible in Siemens Inveon based-images but not visible in MIRRORS images is due to the limited radial (z) FOV of the MIRRORS system which stops at the liver.
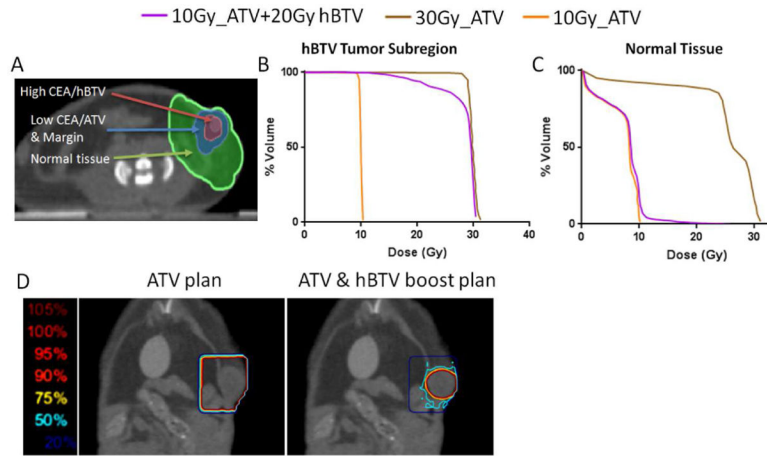
Fig. 10.
Dose targeting based on hBTV. (A) Regions of the anatomical target volume with 2 mm margin (ATV) with high ^{64}Cu-DOTA-M5A activity or highly active biological target volume (hBTV) (pink), low ^{64}Cu-DOTA-M5A activity regions of the ATV plus a 2 mm margin volume (blue), and normal tissue volume surrounding the tumor (green) are shown for a CBCT slice. High activity hBTV regions had voxel activities approximately 1.5-fold greater than the mean activity of the ATV plus margin volume. (B) Dose volume histograms of the hBTV when simulating 10 Gy, and 30 Gy dose ATV based treatment plans as well as the dose volume histogram of the hBTV for 10 Gy dose treatment to the ATV with a 20 Gy boost to the hBTV are shown. (C) The dose volume histograms of the nearby normal tissue when simulating 10 Gy, 30 Gy dose treatments to the ATV as well as 10 Gy dose treatment to the ATV with a 20 Gy boost to the hBTV are shown. (D) A comparison of isodose lines for 30 Gy ATV only based (left) treatment plan and 10 Gy ATV with a 20 Gy boost to the hBTV based treatment plan (right). Isodose lines are displayed on the same coronal CBCT slice. A large reduction in normal tissue dose with minimal comprise in hBTV dose coverage is observed when using molecular image guided radiation therapy (MIGRT) based treatments. Doses were calculated at the center of the corresponding target volumes.

TABLE 1

NEMA NU4 – 2008 IMAGE QUALITY PARAMETERS.

Image quality parameters	Values for NEMA Phantom
RC (%STD) 1 mm	0.135 (22.67%)
RC (%STD) 2 mm	0.162 (16.22%)
RC (%STD) 3 mm	0.319 (12.18%)
RC (%STD) 4 mm	0.56 (10.01%)
RC (%STD) 5 mm	0.80 (9.08%)
Uniformity mean	4.896
Uniformity max.	5.971
Uniformity min.	3.102
Uniformity %STD	40.83%
SOR (%STD) water	0.286 (16.25%)
SOR (%STD) air	0.392 (6.66%)

TABLE 2

<small>Data acquisition and image reconstruction conditions for the ^{64}Cu-DOTA-M5A imaging Of Mouse 1.</small>

Parameters	Siemens Inveon PET/CT	Hamamatsu PET insert
Crystal material	LSO	LFS
Crystal size	1.5 mm × 1.5 mm × 10 mm	4.14 mm × 4.14 mm × 20 mm
Crystal array	20 × 20	12 × 12
Radial FOV	127 mm	53.1 mm
Bore diameter	120 mm	101.6 mm
Initial total activity	8.12 µCi	4.59 µCi
Scan time	60 min	54 min
Energy window	350–650 keV	> ~100 keV
Coincidence window	3.475 ns	3 ns
PET spatial resolution	1.4 mm	2.6 mm
Data corrections	dead time, radial arc correction	-
Total coincidences used for reconstruction	9,024,507	~600,000